RESEARCH ARTICLE
PLANETARY SCIENCES

Earth and Planetary Physics
4: 550–564, 2020
doi: 10.26464/epp2020062

The diurnal transport of atmospheric water vapor during major dust storms on Mars based on the Mars Climate Database, version 5.3

Jing Li[1,2], ZhaoPeng Wu[1,4,5*], Tao Li[2,5], Xi Zhang[3], and Jun Cui[1,4,5]

[1]Planetary Environmental and Astrobiological Research Laboratory, School of Atmospheric Sciences, Sun Yat-sen University, Zhuhai Guangdong 519082, China;

[2]Chinese Academy of Sciences Key Laboratory of Geospace Environment, School of Earth and Space Sciences, University of Science and Technology of China, Hefei 230026, China;

[3]Department of Earth and Planetary Sciences, University of California Santa Cruz, Santa Cruz, California 95064, USA;

[4]Chinese Academy of Sciences Key Laboratory of Lunar and Deep Space Exploration, National Astronomical Observatories, Chinese Academy of Sciences, Beijing 100012, China;

[5]Chinese Academy of Sciences Center for Excellence in Comparative Planetology, Hefei 230026, China

Key Points:

- The diurnal transport of atmospheric water vapor is common during major dust storms on Mars, based on the Mars Climate Database 5.3
- The migrating diurnal tide dominates the diurnal transport of water vapor during most of the major dust storms
- Tidal transports during Martian year (MY) 25 spring and MY 28 summer global dust storms may have opposite effects on water escape

Citation: Li, J., Wu, Z. P., Li, T., Zhang, X. and Gui, J. (2020). The diurnal transport of atmospheric water vapor during major dust storms on Mars based on the Mars Climate Database, version 5.3. *Earth Planet. Phys.*, *4*(6), 550–564. http://doi.org/10.26464/epp2020062

Abstract: In recent studies of the Martian atmosphere, strong diurnal variation in the dust was discovered in the southern hemisphere during major dust storms, which provides strong evidence that the commonly recognized meridional transport process is driven by thermal tides. This process, when coupled with deep convection, could be an important part of the short-term atmospheric dynamics of water escape. However, the potential of this process to alter the horizontal distribution of moist air has not been systematically investigated. In this work, we conducted pre-research on the horizontal transport of water vapor associated with the migrating diurnal tide (DW1) at 50 Pa in the upper troposphere during major dust storms based on the Mars Climate Database (MCD) 5.3, a state-of-the-art database for Martian atmospheric research that has been validated as simulating the relevant short-period atmospheric dynamics well. We found westward-propagating diurnal patterns in the global water vapor front during nearly all the major dust storms from Martian years (MYs) 24 to 32. Statistical and correlation analyses showed that the diurnal transport of water vapor during global and A-season regional dust storms is dominated by the DW1. The effect of the tidal transport of water vapor varies with the types of dust storms in different seasons. During regional dust storms, the tidal transport induces only limited diurnal motion of the water vapor. However, the horizontal tidal wind tends to increase the abundance of daytime water vapor at mid- to low latitudes during the MY 28 southern summer global dust storm while decreasing it during the MY 25 southern spring global dust storm. The tidal transport process during these two global dust storms can induce opposite effects on water escape.

Keywords: Martian atmosphere; thermal tides; water vapor; dust storms; water escape

1. Introduction

The existence of water on an extraterrestrial planet like Mars is significant because it indicates the potential for life. While there is widespread water ice in the atmosphere (Hinson and Wilson, 2004; Wilson et al., 2007; McCleese et al., 2010) and perennial water ice in the polar caps (Bibring et al., 2004; Hale et al., 2005; Bandfield, 2007), Mars appears to have no perennial liquid water on its surface at present (Haberle et al., 2001; Martin-Torres et al., 2015). However, the presence of fluvial features implies that liquid water was once present on the surface of Mars (McKay, 1997). Previous studies have suggested that Mars was substantially warmer and wetter in the past than at present (Pollack et al., 1987; Craddock and Howard, 2002). Therefore, Mars would have experienced substantial climate change and water loss throughout its history.

Multiple mechanisms could account for the water loss from Mars, among which water escape from the atmosphere to space is an important way and is ongoing to the present day (Nair et al., 1994;

Correspondence to: Z. P. Wu, wuzhp9@mail.sysu.edu.cn
Received 31 MAR 2020; Accepted 19 JUN 2020.
Accepted article online 01 SEP 2020.

Jakosky and Phillips, 2001). The main mechanism is suggested to be Jeans escape of hydrogen sourced from the photolytic destruction of water vapor in the atmosphere, and the escape rate shows seasonal variability (Jeans, 1921; Zahnle et al., 2008; Chaffin et al., 2014). Previous studies have attributed this seasonal variability to the seasonal variation in water vapor sources detected in the middle atmosphere (Chaffin et al., 2017). Using multiannual observational estimates of water content and dust from Mars Climate Sounder (MCS) data, Heavens et al. (2018) suggested that deep convection during Martian dust storms could transport water to the middle atmosphere, which would explain the seasonal variability of the water vapor source. However, the short-term dynamic process of transporting water content to a high altitude is not yet clearly understood in detail. In a recent observational study, Vandaele et al. (2019) discovered the rapid vertical transport of dust and water to high altitudes from the middle to high latitudes within only a few days during global dust storms, which makes the short-term atmospheric dynamic process on Mars intriguing.

For many years, studies of the Martian middle and lower atmosphere relied heavily on observational data from space-based satellites and ground-based landers and rovers (Smith, 2008). However, most of the satellites, such as the Mars Global Surveyor, Mars Odyssey, and Mars Reconnaissance Orbiter, are in quasi-polar sun-synchronous orbits, which restrains the temporal coverage of their observations to two local times (LTs) per Martian day (referred to as a "sol"). Ground-based instruments can make continuous measurements, but only at local sites. And although comprehensive general circulation models (GCMs) can simulate the day-to-day and diurnal variations of the atmosphere, these results have not yet been fully validated by observations. Therefore, the short-term dynamic process within a sol, especially in the global view, is still poorly understood.

However, the cross-track observations of the MCS can increase the LT coverage and enable detailed study of the short-term dynamics, such as thermal tides (Kleinböhl et al., 2013; Wu ZP et al., 2015). Wu ZP et al. (2020) demonstrated that, driven by the tidal wind and especially the meridional wind, zonally distributed dust fronts in the upper troposphere can slosh back and forth in a wide latitudinal range during major dust storms. In that case, moist air from the summer polar cap can be rapidly transported on the nightside to the middle latitudes. The tidal transport of water vapor has been validated with the help of the Mars Climate Database, version 5.3 (MCD 5.3), a state-of-the-art database of meteorological fields derived from GCM numerical simulations (Millour et al., 2018). This water supply, if entrained by dusty deep convection at mid- to low latitudes, will effectively transport water from the summer polar cap to the middle atmosphere, where it can enhance the hydrogen source through photodissociation. Wu ZP et al. (2020) have qualitatively shown the tidal transport of water vapor during Martian years (MYs) 28 to 34. Yet the relationship between the meridional motion of water vapor and the tidal wind requires a quantitative investigation. Furthermore, the possibility of coupling between the horizontal tidal wind and vertical deep convection during different types of major dust storms has not been discussed.

The column abundance of water vapor has been observed for years with various instruments, and it exhibits distinct seasonal and spatial patterns (Trokhimovskiy et al., 2015). The vertical distribution of high-altitude water vapor, though important for the understanding of hydrogen escape rate variations, has rarely been measured in the past (Fedorova et al., 2018). The MCS data set, although it has good vertical resolution and LT coverage, has no retrievals for water vapor. Therefore, because of the lack of diurnal measurements of global water vapor and wind field profiles, it is impossible to directly analyze their relationship at a certain atmospheric layer (e.g., the upper troposphere, ~20 to 40 km) from any available observational data. However, the well-simulated column-integrated water vapor distribution and its seasonal variation from the MCD have been validated by observations (Navarro et al., 2014). In addition, as validated by Wu ZP et al. (2020), the MCD 5.3 can simulate the horizontal wind field well in the upper troposphere of the southern hemisphere during major dust storms. Driven by this wind field, the simulated water vapor in the MCD 5.3 manifests a diurnal motion in the meridional direction, as shown in Figure 1, which highly resembles the observed diurnal motion of the dust front shown in Supplementary Fig. 6 by Wu ZP et al. (2020). Therefore, it is feasible to conduct a pre-research study on the horizontal transport of water vapor during various major dust storms based on the MCD 5.3. Such a survey is not only able to examine the quality of the water transport simulation in the MCD 5.3, but also to guide the choice of dust storms to focus on in future observations to study the short-period horizontal dynamics. In this work, we quantitatively investigate the relationship between the meridional wind and the diurnal motion of water vapor in all major dust storms from MYs 24 to 32 and discuss the effect of the tidal transport process in different dust storms and seasons. This analysis has not been done in previous studies. Section 2 gives a brief introduction to the MCD 5.3 data set, the major dust storms, and the methods used in this study. Section 3 shows the main statistical results for the relationship between the meridional wind and the distribution of water vapor. Section 4 discusses the effects of the tidal transport of water vapor in different seasons. Finally, Section 5 gives a summary.

2. Data and Methods

2.1 The Mars Climate Database 5.3

The MCD 5.3 is a state-of-the-art database of meteorological fields for the Martian atmosphere (Millour et al., 2018). It provides all primary meteorological fields, such as winds, temperature, pressure and dust, water vapor, and water ice content, which are from the Martian GCM developed at the Laboratoire de Météorologie Dynamique (Forget et al., 1999) and have been validated by using the latest observational data from the primary spacecraft. The Laboratoire de Météorologie Dynamique GCM includes advanced dust cycle and water cycle models (Madeleine et al., 2011; Navarro et al., 2014) to simulate the thermodynamic process of dust storms and the microphysics of dust and water particles. The solid–gas phase transition of airborne water and its transport during dust storms are theoretically self-consistent and have been validated by available observations. The MCD 5.3 provides simulated Martian meteorological information from MYs 24 to 32 driven correspondingly by the spacecraft-derived dust climatology for each

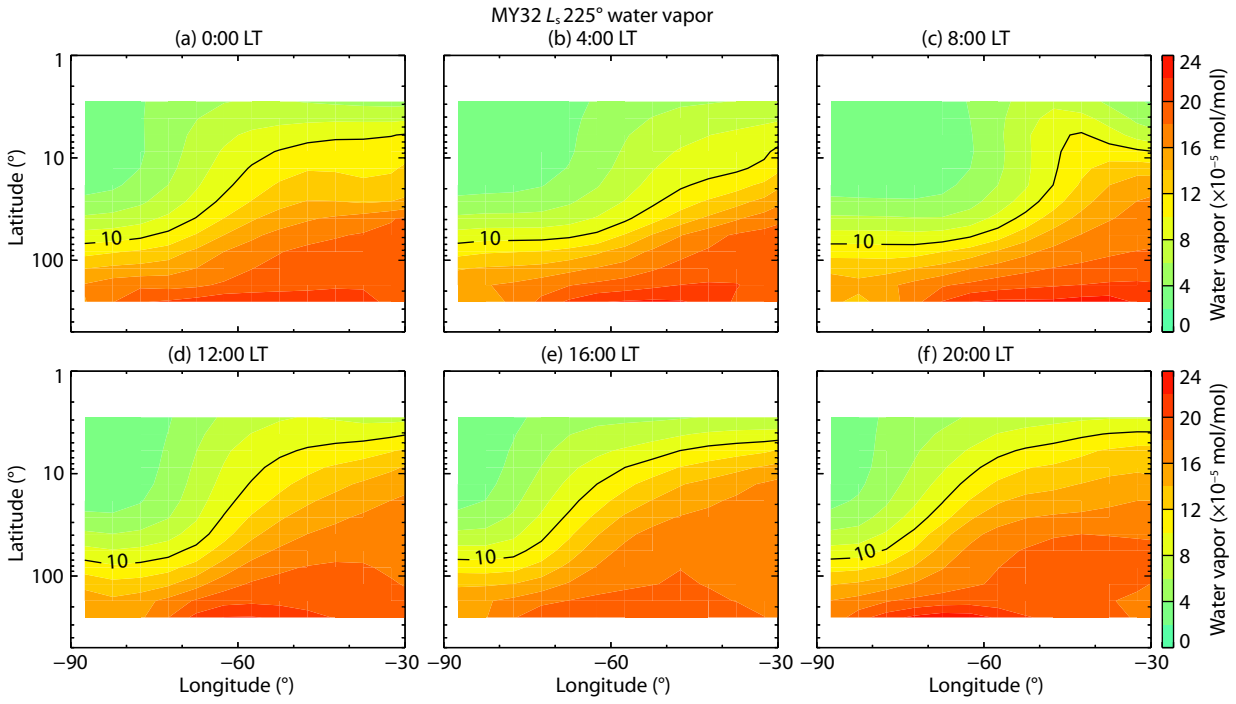

Figure 1. Diurnal variation of the vertical and meridional structures of the high-latitude water vapor mixing ratio during an A regional dust storm at a solar longitude (L_s) of 225° in MY 32. The local time (LT) value is labeled at the top of each panel. The black solid contour line in each panel shows the typical water vapor front.

MY (Montabone et al., 2015). In this work, the meridional wind and water vapor data of these 9 MYs were used. Additionally, water vapor that manifests a prominent meridional motion is mainly between 10 to 70 Pa, as shown in Figure 1, which is similar to the dust front reported by Wu ZP et al. (2020). This provides further validation for the simulated horizontal wind field in the upper troposphere and the feasibility of evaluating the horizontal motion of water vapor with the MCD 5.3. In this work, a pressure level of 50 Pa was chosen, as in Wu ZP et al. (2020), to perform the entire analysis. It should be noted that the simulated column-integrated water vapor of the MCD has been validated with observations by Navarro et al. (2014), but not for each pressure level. Therefore, we focus more on the extent of the wind-induced horizontal motion of water vapor rather than the exact amount of water vapor that can be transported.

2.2 Major Dust Storms from Martian Year 24 to 32

Although dust exists in the lower atmosphere of Mars throughout the entire MY, it shows significant seasonal variation. Driven by the significant increase in insolation, the amount of dust is relatively high during the perihelion seasons (i.e., southern spring and summer; Kass et al., 2016). These seasons are also known as those that usually last from a solar longitude (L_s) of 180° to 360°. Major dust storms include planet-encircling global storms and three types (A, B, and C) of large regional dust storms during the dust storm season (Kass et al., 2016). They have significant influences on the global-scale atmospheric structure and circulation (Smith, 2008; Kass et al., 2016). The A-season storm tends to be initiated during the middle of the southern spring and to end by the southern summer solstice. It can warm the atmosphere at most latitudes in the southern hemisphere. The B-season storm begins just after the perihelion and reaches a peak around the southern summer solstice. Because it occurs only in the southern polar region, the B-season storm is found to have a limited northern dynamic effect. The C-season storm usually begins after the end of the B storm and is shorter than the A and B storms. It is weaker and occurs irregularly year by year. The A and C storms are very much alike, and both have northern responses by enhancing the Hadley circulation. The B storm is not considered in this work because it has limited dynamic effects, especially on the atmospheric diurnal variation (Wu ZP et al., 2020). According to previous visible imaging studies, the majority of A and C storms may originate from northern middle-latitude local storms that flush across the equator into the southern hemisphere (Wang HQ and Richardson, 2015). Under some unknown conditions, regional and other smaller dust storms in some MYs can grow explosively to form a global-scale dust storm — a splendid form of atmospheric interannual variability on Mars (Shirley and Mischna, 2017). These global dust storms occur at irregular MY intervals, and only two events have been captured during the 9 MYs considered in this work. Details on the occurrence of each regional dust storm from MYs 24 to 32, excluding global dust storms, can be found in Kass et al. (2016). In addition, the climatology of the dust optical depth, including periods of all the regional and global dust storms in the 9 MYs, is available on the MCD website (Montabone et al., 2015). The approximate period of occurrence of the global dust storms can be determined by considering the significant enhancement of the dust optical depth during the storm time. In Table 1, we summarize the approximate periods of the A and C regional and global dust storms during MYs 24–32. All L_s ranges are rounded and enlarged to reflect the limited sample size. Note that C storms in some MYs are quite small and are not listed in the table. Also note that these

Table 1. The chosen L_s duration of all the major dust storms from MYs 24 to 32.

Martian year	L_s duration		
	Global storm	A storm	C storm
24	—	225°–240°	—
25	190°–250°	—	—
26	—	210°–230°	315°–325°
27	—	225°–245°	310°–320°
28	265°–305°	—	—
29	—	230°–250°	310°–325°
30	—	235°–250°	315°–325°
31	—	210°–230°	315°–325°
32	—	220°–235°	310°–325°

periods are used only in the statistical analysis of this work and are not exactly the same as those defined by Kass et al. (2016). Specifically, the durations shown in Table 1 cover the entire rising phase (from start to peak time) and the peak time but only partially cover the ending phase (from peak to end time) of the dust storms. The durations chosen in this way correspond to the statistical sampling strategy, which is discussed in Section 3.2. During the entire dust storm season, and especially during major dust storms, the increased temperature in the southern hemisphere tends to promote the transition from water ice to water vapor in the troposphere (McCleese et al., 2010; Haberle et al., 2017). The overall water ice abundance in the MCD is much lower than the water vapor abundance by an order of magnitude (not shown). Therefore, the data analysis in this work is mainly focused on water vapor.

2.3 Extraction of the Migrating Diurnal Tide

Thermal tides are the dominant global-scale waves in the rapidly rotating atmosphere of planets such as the Earth, Mars, and Venus. Driven by solar heating, the period of a thermal tide corresponds to the subharmonics of a solar day, such as 24, 12, and 8 hours (Forbes, 1995). On Mars, the main excitation sources of thermal tides are the widely distributed dust and water ice (Wu ZP et al., 2015, 2017). Once excited, the global-scale waves propagate zonally and vertically, and they transport energy and momentum away from the wave source. Therefore, tides can be regarded as waves traveling in the zonal and vertical directions according to the following trigonometric function (Wu ZP et al., 2015, 2020):

$$\Phi(\lambda,\theta,p,t)=\sum_{\sigma,s}\Phi_{\sigma,s}(\theta,p)\cos(\sigma t-s\lambda+\varphi_{\sigma,s}), \tag{1}$$

where Φ can be temperature, wind, density, or the abundance of aerosols; λ, θ, p, and t are longitude, latitude, pressure, and universal time (UT, an LT of 0° longitude), with λ and t in units of radians; σ is the harmonic number (1 indicates diurnal, 2 indicates semidiurnal); s is the zonal wavenumber, where positive s indicates eastward propagation and negative s indicates westward propagation; and $\Phi_{\sigma,s}(\theta,p)$ and $\varphi_{\sigma,s}$ are the amplitude and phase of a certain wave mode (σ, s). The (1, −1) mode, also known as the migrating diurnal tide (DW1), is one of the most important tides on Mars. It was also found to be the dominant wave mode in the southern hemisphere during major dust storms (Guzewich et al., 2014; Wu ZP et al., 2020). The DW1 propagates westward at a phase speed the same as the subsolar point. This can also be recognized if we substitute (1, −1) into $\sigma t-s\lambda$ and get $t+\lambda$, which is the same expression for LT $\hat{t}=t+\lambda$ from UT t. In other words, the zonal migration of the meteorological fields (e.g., the horizontal wind and water vapor) dominated by the DW1 is dependent on only one variable, namely, the LT, as shown in Figure 2. The fields in Figure 2 are located at the same solar longitude and pressure level as those in Supplementary Fig. 10a, 10b of Wu ZP et al. (2020), which they demonstrated are dominated by the DW1. The direction of the winds at mid- to low latitudes of the southern hemisphere is equatorward around midnight and poleward around noon, coupled as well with the transport of global water vapor (Figure 2a–2d). Their spatial distribution patterns at the same LT $\hat{t}$ remain almost unchanged, exhibiting significant diurnal variation. Note that the LT $\hat{t}$ is equivalent to the longitude λ at 0 UT. Therefore, the amplitude and phase of the diurnal tide can be determined by applying a nonlinear least-squares fit to the global distributions of the meteorological fields at 0 UT, as shown in Figure 2a, with the following function (Wu ZP et al., 2015, 2017):

$$\Phi(\theta,p)\approx\Phi_{1,-1}(\theta,p)\cos(\lambda+\varphi_{1,-1})+C, \tag{2}$$

where $\Phi_{1,-1}$ and $\varphi_{1,-1}$ are the amplitude and phase of the DW1 and C represents the background on which the DW1 component is superimposed. Hereafter in this work, all the statistics for and analyses of the amplitude and phase of the DW1 are based on the global distributions of the corresponding meteorological fields at 0 UT.

3. Results

3.1 Diurnal Motion of Water Vapor Induced by the Tidal Meridional Winds

To quantitatively determine the characteristics of the diurnal motion of water vapor and its relationship to the meridional tidal wind, the DW1 amplitudes and phases were calculated by using the method described in Section 2.3. Taking the situation in Figure 2a as an example, we show the meridional distribution of the amplitudes and phases of the diurnal components of water vapor and meridional wind (hereafter referred to as the water vapor DW1 and meridional wind DW1) in Figure 3.

The water vapor abundance shows a sharp gradient and forms a water vapor front at mid- to high latitudes (Figure 3a), a phenomenon similar to the dust front described by Wu ZP et al. (2020). The water vapor front has a clear trigonometric-function pattern versus longitude (shown as the yellow ribbon). Wu ZP et al. (2020) suggested that the atmosphere in the upper troposphere at southern mid- to high latitudes is dominated by a horizontal motion during major dust storms and that this horizontal motion is the main cause of the strong diurnal variation in airborne dust and water vapor (also shown in Figure 1). As expected, the peak amplitude of the water vapor DW1 is located at ~63°S (Figure 3c), near the central latitude of the water vapor front (i.e., the averaging latitude of the yellow ribbon). The central latitude

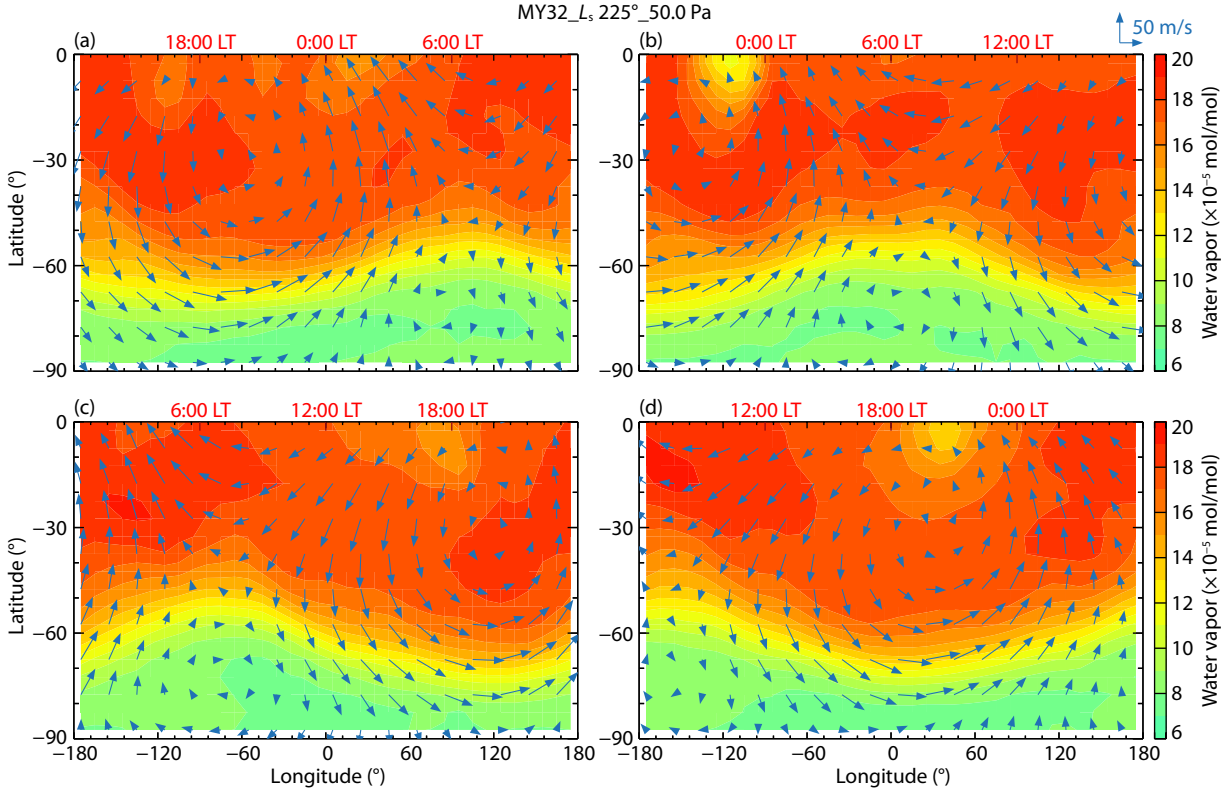

Figure 2. Diurnal variation of the horizontal wind fields (blue vectors) and water vapor distribution (colors) at 50 Pa, L_s of 225° in the southern hemisphere during the A regional dust storm in MY 32. (a) 0 universal time (UT); (b) 6 UT; (c) 12 UT; (d) 18 UT. LT, local time.

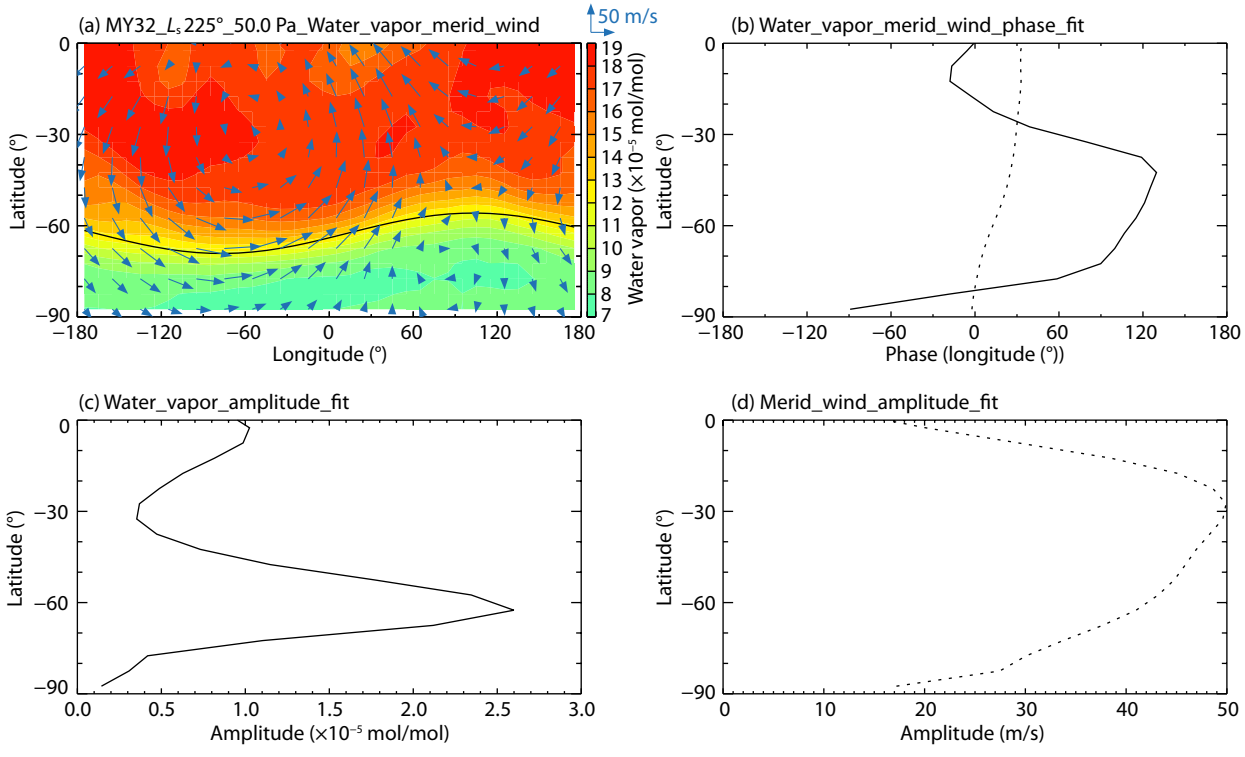

Figure 3. Meridional variations of the DW1 phases (b) and amplitudes (c, d) of water vapor (solid lines in b and c) and meridional wind (dotted lines in b and d) at 50 Pa, L_s of 225° during the A regional dust storm in MY 32 (a).

of the water vapor front is dependent on the meridional distribution of the water vapor, which is seasonally varied, as discussed later in Section 4.

The phases of the meridional wind DW1 and the water vapor DW1 are defined as the longitude (or the corresponding LT when UT = 0) of the maximum northward wind and minimum water vapor, respectively. As shown in Figure 3b, the phase of the meridional wind DW1 is near 0° longitude (0 LT) with a slight latitudinal change. This phase corresponds to the wind vector distribution in Figure 2a, showing that the direction of the wind is equatorward around midnight and poleward around noon. This wind pattern is dominated by the DW1 tide, and the thermal dynamic process behind it can be accurately described by classical tidal theory (Chapman and Lindzen, 1970; She CY et al., 2016; Wu ZP et al., 2020). The phase of the water vapor DW1 is relatively complicated. At mid- to high latitudes where the amplitude of the water vapor DW1 is large (40°S–70°S), the phase of the water vapor DW1 is around 90° longitude (6 LT), lagging the phase of the meridional wind DW1 by one-fourth of the DW1 period. This result provides strong evidence that the diurnal variation of the water vapor is mainly caused by the meridional wind DW1. The phase relationship between the meridional wind and water vapor can be understood more intuitively by focusing on the latitude where the strongest diurnal variation of water vapor occurs, namely, the central latitude of the water vapor front.

The first and primary step in determining the water vapor front is to find the typical water vapor abundance at the water vapor front. This can be identified as the value at the latitude of the sharpest latitudinal gradient of the water vapor abundance. Here, under the circumstance that the diurnal variation of water vapor is caused by the diurnal meridional motion, it is also appropriate to use the background constant C in Equation (2) at the latitude of the peak amplitude of the water vapor DW1 as the typical value of the water vapor front. We can then locate the latitude of the typical water vapor abundance for each longitude and obtain a 1-D latitude array representing the location of the water vapor front. Finally, the nonlinear least-squares fit with Equation (2) is applied to this latitude array to obtain the amplitude and phase of the water vapor front DW1, which describes the characteristics of the meridionally diurnal motion of the water vapor front. The phase of the water vapor front DW1 is defined as the longitude (or the corresponding LT when UT = 0) when the water vapor front reaches the northernmost point. The black line in Figure 3a shows the fitted water vapor front when using the procedure described above. The fitted water vapor front matches the yellow ribbon pattern well. As expected, the phase of the water vapor front DW1 also lags behind that of the meridional wind DW1 by roughly one-fourth of the DW1 period (not shown). To illustrate the phase difference, we can choose a water vapor parcel at the water vapor front and consider only its meridional motion with the meridional wind. The speed variation of this parcel should then be in the form of a cosine function at a period of one sol. Therefore, the displacement of the water vapor parcel can be simplified as an integration of the speed cosine function, which lags just $\pi/2$ radian in phase (corresponding to 6 hours or 90° longitude for the DW1). In contrast, the zonal transport of water vapor by the zonal wind — not only the tidal wind but also the thermal gradient wind (Wu ZP et al., 2020) — can modulate the integration time of the meridional motion and thus alter the magnitude and shape of the cosine pattern of the water vapor front. However, because the zonal wind during regional dust storms (usually below 80 m/s at 50 Pa) is moderate compared with the horizontal phase speed (~250 m/s) of the DW1, the distortion of the cosine pattern is limited, as shown in Figure 2. In the following sections, the diagnostic procedures described above are performed on all the major dust storms from MYs 24 to 32 for further analysis.

3.2 Diurnal Variations of the Water Vapor During All the Major Dust Storms

Wu ZP et al. (2020) clearly showed the diurnal motion of water vapor in the southern hemisphere during an A-season regional dust storm in MY 32 (see also Figures 1 and 2 in this work) and a global dust storm in MY 28. In this section, we investigate this phenomenon from a broader perspective to determine whether the diurnal variation of water vapor is prominent during all the major dust storms.

Note that the period when each storm occurs contains three phases: the rising, peak, and ending phases. The atmospheric temperature at 50 Pa usually increases rapidly at the onset, reaches the highest point at the peak time, and then decreases slowly at the ending phase (Kass et al., 2016). In this work, we focus on the general relationship between the meridional wind and water vapor distribution of multiple major dust storms and thus disregard the detailed evolution of a certain event. First, the L_s range for each dust storm is roughly defined based on the temporal information from Kass et al. (2016) and Montabone et al. (2015). We then manually check whether the pattern of diurnal motion of the water vapor shown in Figure 2 or 3a is prominent throughout this L_s range. This is done to ensure (1) that the period of the simulated dust storm matches the observed period and (2) that the horizontal diurnal motion of water vapor occurs over the entire period of a major dust storm. Generally, our manual check confirmed that the simulated diurnal motion of water vapor occurs during the entire period of the observed dust storm. However, the extent of the diurnal motion during the ending phase of each dust storm remains small and nearly the same. As indicated in the supporting file of Kass et al. (2016), the rising phase of a major dust storm is usually much shorter than the ending phase. Thus, if the entire period of a dust storm was sampled, the large number of samples in the ending phase would have a weak effect and nearly the same extent of water vapor diurnal motion. However, statistical analysis of the relationship between the meridionally diurnal motion of the water vapor front and the meridional tidal wind requires strong sampling diversity, which would be weakened by a surplus of similar samples. Consequently, we chose to sample the entire rising phase and the peak time of a dust storm but to partially sample its ending phase (less than half of the ending phase in some cases). The chosen periods of all the major dust storms from MYs 24 to 32 are listed in Table 1. By uniformly sampling the chosen L_s duration of the dust storms, we included nearly all three phases in our statistics. Specifically, 8–10 samples were chosen for the global dust storms, 5–6 were chosen for the A regional dust storms, and 3–4 were chosen for

the C regional dust storms. Consequently, the variations in the meridional wind and water vapor across nearly the entire dust storm phase would be represented in the results.

Approximately 70 samples (each corresponding to an L_s) were used in our investigation. In general, the pattern of diurnal variation is prominent in nearly all of them. Figure 4 presents typical examples of diurnal variation chosen for different A and C regional and global dust storms. The results show similar diurnal patterns in the wind and water vapor fields in all other major dust storms, such as those in MY 32 (Figures 2a, 3a). Using the method of determining the water vapor front described in the previous section, we also located the water vapor fronts, as shown by the black lines for all the examples. The magnitudes of diurnal variation in the meridional wind and water vapor fields differ for different dust storms. Specifically, the diurnal variations during global dust storms (Figures 4k, 4l) are much stronger than those during regional dust storms (Figures 4a–4j) when their wind vectors and water vapor fronts are compared. Figure 4a–4j are sorted by L_s. By comparing different L_s and different MYs, we found seasonal and interannual variations in the water vapor abundance and the central latitude of the water vapor front.

3.3 Correlation Between Water Transport and the Meridional Wind

As discussed in Section 3.1, the water vapor near the water vapor front usually exhibits the most prominent diurnal variation in the meridional direction, which makes the water vapor front the ideal location for a quantitative investigation of the relationship between the meridional wind and the corresponding water vapor

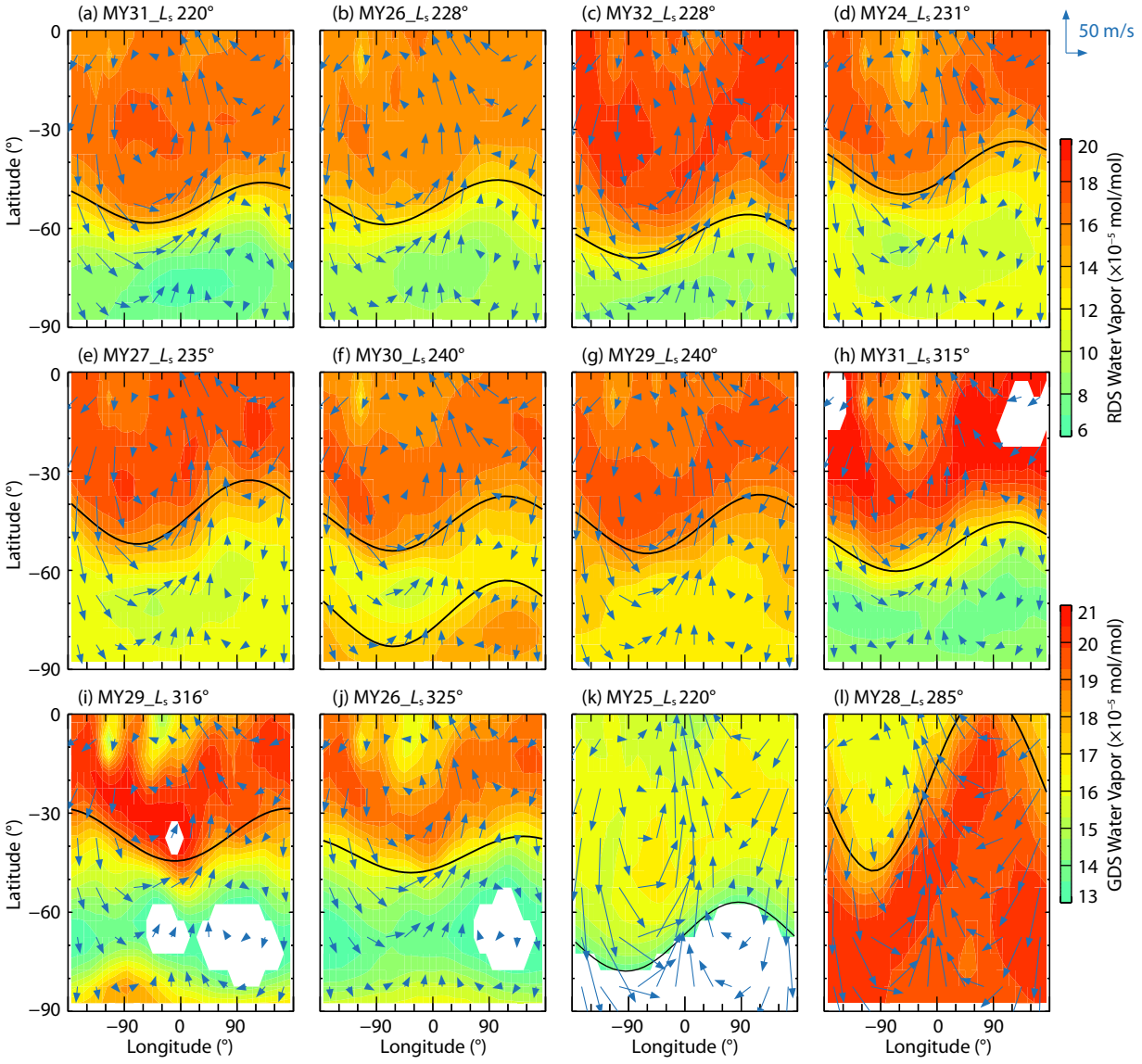

Figure 4. Typical diurnal variations in the water vapor (color) and wind fields (vectors) during multiple major dust storms. Panels (a)–(j) are during regional dust storms (RDS) in order of L_s, in which panels (a)–(g) are during A regional dust storms and panels (h)–(j) are during C regional dust storms. Panels (k) and (l) are during global dust storms (GDS). Note that the regional dust storms and global dust storms are represented by different color bar ranges. The blank areas in some of the plots are beyond the color bar range. The black curve in each plot represents the fitted water vapor front.

transport. In this section, we discuss the statistical and correlation analyses that were performed for the water vapor abundance–water vapor front DW1 and the meridional wind DW1. Specifically, the amplitude correlation analysis included (1) the relationship between the amplitude of the water vapor front DW1 (described in Section 3.1, in units of latitude degrees (°)) and the amplitude of the meridional wind DW1 (in units of m/s) at the central latitude of the corresponding water vapor front, (2) the relationship between the amplitude of the water vapor abundance DW1 (e.g., the maximum in Figure 3c, in units of mol/mol), and the amplitude of the meridional wind DW1, both at the central latitude of the water vapor front. The results of the amplitude correlation analysis are illustrated in scatter diagrams (Figures 5 and 7). For the phase correlation analysis, the statistical results of the phase differences between the water vapor abundance–water vapor front DW1 and the meridional wind DW1 are shown in Figure 6.

Before the analysis, all the samples were divided into three latitude zones (high latitudes [–90°, –60°], middle latitudes [–60°, –30°], and low latitudes [north of –30°]) based on the central latitude of the water vapor front. As shown in Figure 5, the water vapor fronts of different types of dust storms tended to be distributed in different latitudes, with middle to high latitudes for the A regional storms, middle latitudes for the C regional storms, and high or low latitudes for the global storms. This tendency is related to the season in which different dust storms occur and the corresponding meridional distribution of water vapor, which are discussed in Section 4. As shown in Figure 5, the maximum meridional motion range within one sol of the water vapor front (2× the amplitude of the water vapor front DW1) varies with different latitude zones as well, specifically 10°–25° for the middle- and high-latitude zones and 30°–60° for the low-latitude zones. Note that the median meridional motion range of the A regional storms is ~15° (as is this case in Figure 1). This value closely matches the meridional motion range of the dust front in the A regional dust storm of MY 33 observed by Wu ZP et al. (2020).

Under the ideal condition that water vapor is transported meridionally only by the meridional wind DW1, the amplitude of the water vapor front DW1 should be positively correlated with the amplitude of the meridional wind DW1. Given that the amplitude of the meridional wind DW1 across the entire meridional motion range of the water vapor front within one sol is constant and equals the value at the central latitude of the water vapor front, the ratio between the amplitude of the water vapor front DW1 and the amplitude of the meridional wind DW1 could be computed as ~0.24. As shown in Figure 5, a strong positive correlation was found between the mid-latitude A regional dust storm (Figure 5e) and the high-latitude global dust storm (Figure 5d). In these two cases, the amplitude of the water vapor front DW1 shows an increase approximately proportional to the amplitude of the meridional wind DW1, but with a different ratio. The mid-latitude A regional dust storm has a ratio of 0.25, which is very close to that under the ideal condition. However, the high-latitude global

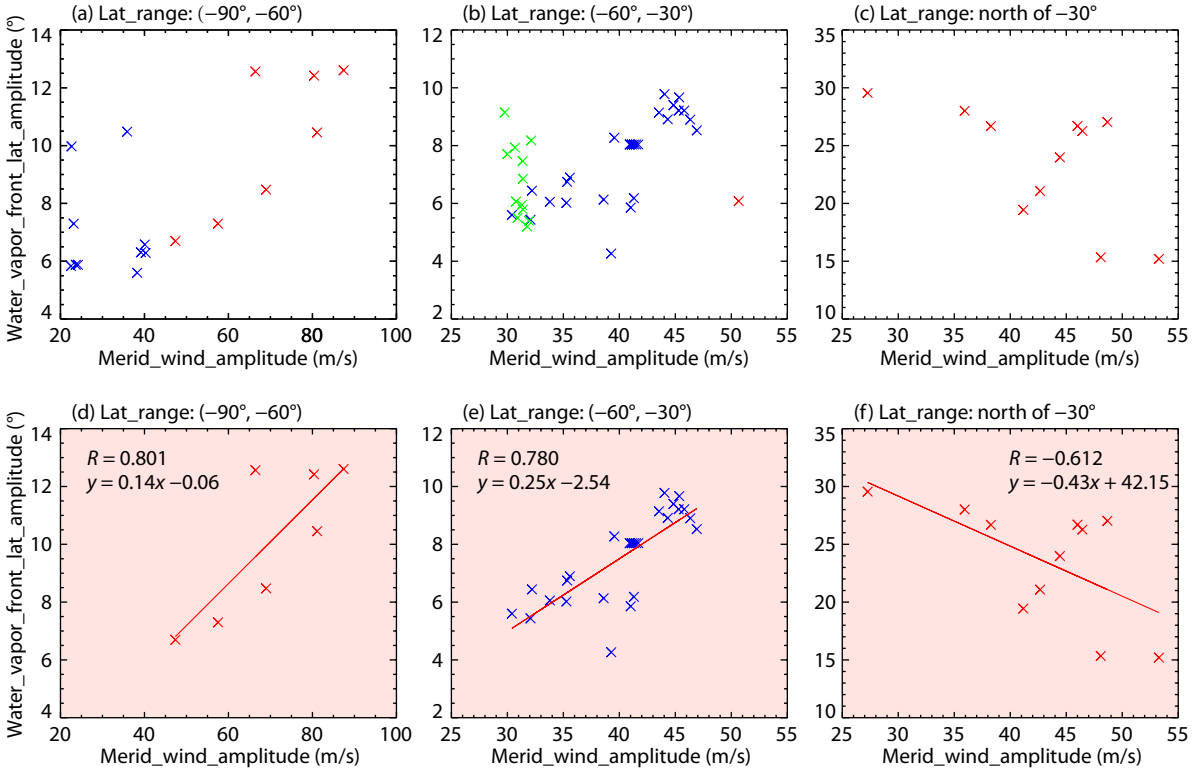

Figure 5. Results of the statistical and correlation analyses for the amplitudes of the meridional wind DW1 (*x*-axis) and the amplitudes of the water vapor front DW1 (*y*-axis). The left, middle, and right columns correspond to latitude zones (–90°, –60°), (–60°, –30°), and (north of –30°). The blue, green, and red crosses represent A and C regional and global dust storms, respectively. Panels (d), (e), and (f) show results of the linear regression analysis for panels (a), (b), and (c), respectively. Note that the results of the linear regression analysis shown here do not include every type of dust storm.

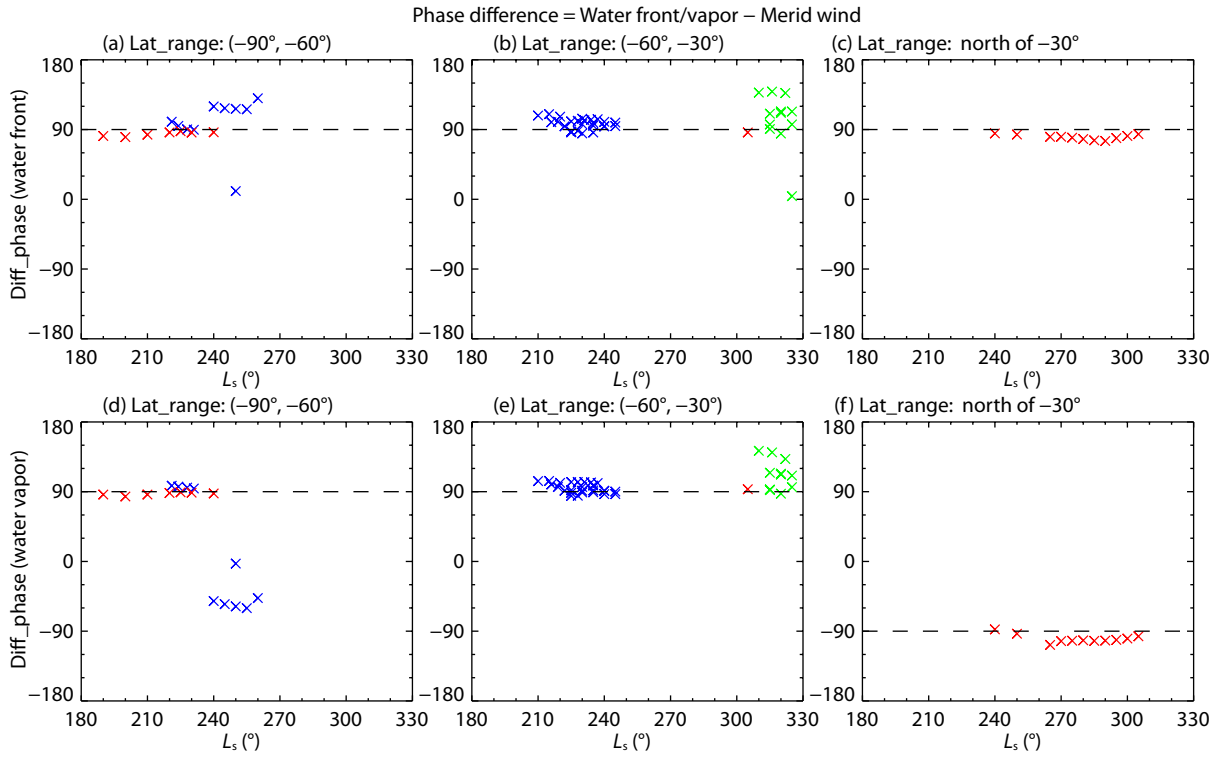

Figure 6. Phase differences of all the examples versus L_s for (a–c) the water vapor front DW1–meridional wind DW1; (d–f) the water vapor abundance DW1–meridional wind DW1. The left, middle, and right columns correspond to the latitude zones (–90°, –60°), (–60°, –30°), and (north of –30°). The blue, green, and red crosses represent A and C regional and global dust storms. Phases of the meridional wind DW1, the water vapor abundance DW1, and the water vapor front DW1 are defined as, respectively, the longitude (local time) of the maximum northward wind, the minimum water vapor, and the northernmost water vapor front.

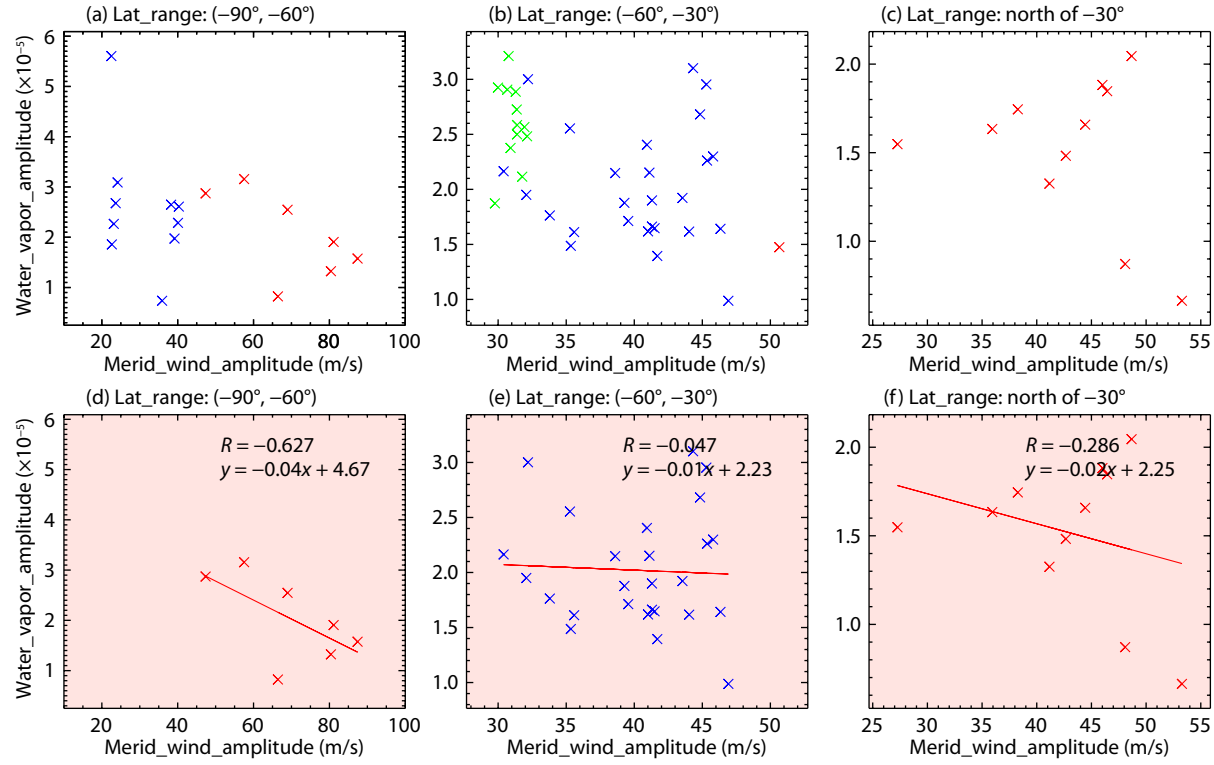

Figure 7. Same as Figure 5 but for the amplitudes of the meridional wind DW1 (*x*-axis) and amplitudes of the water vapor abundance DW1 (*y*-axis).

dust storm has a smaller coefficient of 0.14. This result is probably due to the much higher speed (up to 160 m/s) of the zonal wind at high latitudes during global dust storms (refer to the vectors in Figure 4k, 4l) because the strong zonal wind can greatly reduce the integration time for the meridional wind DW1 and thus shorten the meridional motion. In contrast, the phase relationship statistics show that the water vapor front DW1 lags behind the meridional wind DW1 by ~90° (one-fourth of the DW1 period) in both cases shown in Figure 6a and 6b. This result further confirms the dominant role of the meridional wind DW1 in transporting water vapor meridionally.

Apart from these two cases, however, other cases show no obvious positive correlation in amplitude. In addition, the 90° lag in phase relationship is not well satisfied in most cases except for the low-latitude global dust storm (Figure 6a–6c). The high-latitude A regional dust storms (blue crosses in Figure 5a) have smaller amplitudes of the meridional wind DW1 than those at middle latitudes, but they still retain moderate amplitudes of the water vapor front DW1, which suggests that other processes, such as the polar vortex, may dominate at high latitudes (Kleinböhl et al., 2020). Regarding the low-latitude global dust storms (Figure 5c), two factors should be considered. First, the maximum meridional motion range within one sol is so large (up to 60°) that the assumption of using the amplitude of the constant meridional wind DW1 for the entire meridional motion range could cause nonnegligible bias. Second, the vertical motion induced by thermal tides and slope winds at low latitudes is much stronger than the motion at the southern mid- to high latitudes (Guzewich et al., 2013; Heavens et al., 2014; Wu ZP et al., 2020), which complicates the diurnal variation of water vapor in the low latitudes. The middle-latitude C regional dust storms (Figure 5b) also indicate that the meridional wind DW1 has a weak effect on the motion of water vapor. The amplitude of the water vapor front varies from 5° to 10° latitude, whereas the amplitude of the meridional wind DW1 remains small, at ~32 m/s. Because the C dust storm is shorter and has a weaker thermal impact than the A storm (Kass et al., 2016; Wu ZP et al., 2020), the DW1 tide in the C storm is expected to be smaller as well (compare Figure 9 with Figure 3). As a result, the distribution of water vapor may not be dominated by the DW1 tide. This is reflected in the irregular trigonometric-function pattern for water vapor abundance (shown as the yellow ribbon in Figure 9a). Smaller waves are superimposed on the DW1 wave pattern, which indicates the existence of other tidal or planetary waves with shorter zonal wavelengths. Consequently, the fitted water vapor front shown by the black curve does not match the irregular wave pattern well.

The amplitude relationship between the water vapor abundance DW1 and the meridional wind DW1, both at the central latitude of the water vapor front, is shown in Figure 7. A strong positive correlation in amplitude was not found across all types of dust storms. However, the phase relationship statistic showed results similar to those between the water vapor front DW1 and the meridional wind DW1 (compare Figure 6a, 6b and Figure 6d, 6e). The seeming contradiction for the low-latitude global dust storm shown in Figure 6c and 6f is due to the meridional gradient direction of the water vapor abundance. In Figure 4c and Figure 4l, for example, the water vapor tends to concentrate in the mid- to low latitudes during A regional dust storms (Figure 4c) but to concentrate in the mid- to high latitudes during the MY 28 global dust storm (Figure 4l). Consequently, the water vapor abundance to the north of the water vapor front is larger than that to the south, as shown in Figure 4c, whereas the opposite is the case in Figure 4l. Therefore, the water vapor abundance DW1 in the two examples above are opposite in phase, whereas the water vapor front DW1 in them are in-phase. In short, the phase relationship for water vapor abundance is in accord with that for the water vapor front, which can be treated as evidence for tidal-driven water vapor transport. However, the irregular amplitude relationship indicates that processes other than the meridional wind should also be considered.

Unlike the water vapor front, which represents the relative meridional change in water vapor, the water vapor abundance DW1 is more sensitive to the absolute change in water vapor, which can be affected by several factors. Whereas the overall water ice abundance is smaller than that of water vapor by an order of magnitude, the local day–night phase transition between water vapor and water ice caused by the temperature DW1 may still induce nonnegligible biases. To examine this effect, we considered the total water content (sum of water vapor and water ice) and conducted the same amplitude correlation analysis as above. The result for the water content front DW1 (not shown) is similar to that for the water vapor front DW1 (Figure 5), indicating the insensitivity of the "front," which is a relative quantity. In contrast, the result for the total water content abundance DW1 shows a clearer positive correlation in the middle-latitude A regional storm (Figure 8e) than that for the water vapor abundance DW1 (Figure 7e). Compared with the influence of the diurnal varied water phase transition, the variation in water vapor over a longer time scale may be more prominent. For example, the amplitude relationships of the high-latitude global dust storms shown in Figures 5d, 7d, and 8d are all examples during the MY 25 global dust storm from L_s of 190° to 250° (refer to the L_s ranges in Figure 6a, 6d). The seasonal variation in the water vapor abundance at high latitudes at this long time scale can be up to one order of magnitude (Figure 10). Thus, the aliasing of the seasonal variation can cause huge biases to the results for the amplitude of abundance shown in Figures 7d and 8d.

In this section, we provide the results of the statistical and correlation analyses for the water vapor abundance–water vapor front DW1 and the meridional wind DW1. The phase relationship between them provides direct evidence for the tidally driven meridional transport of water vapor in the middle-latitude A regional dust storms and in the high-latitude and low-latitude global dust storms. Regarding the amplitude relationship, the relative quantity — the amplitude of the water vapor front DW1 — shows a clear positive correlation with the amplitude of the meridional wind DW1, whereas the absolute quantity — the water vapor abundance — is more sensitive to other factors.

4. Discussion — Effect of the Tidal Transport of Water Vapor in Different Seasons

As described in Section 3, the diurnal motion of water vapor asso-

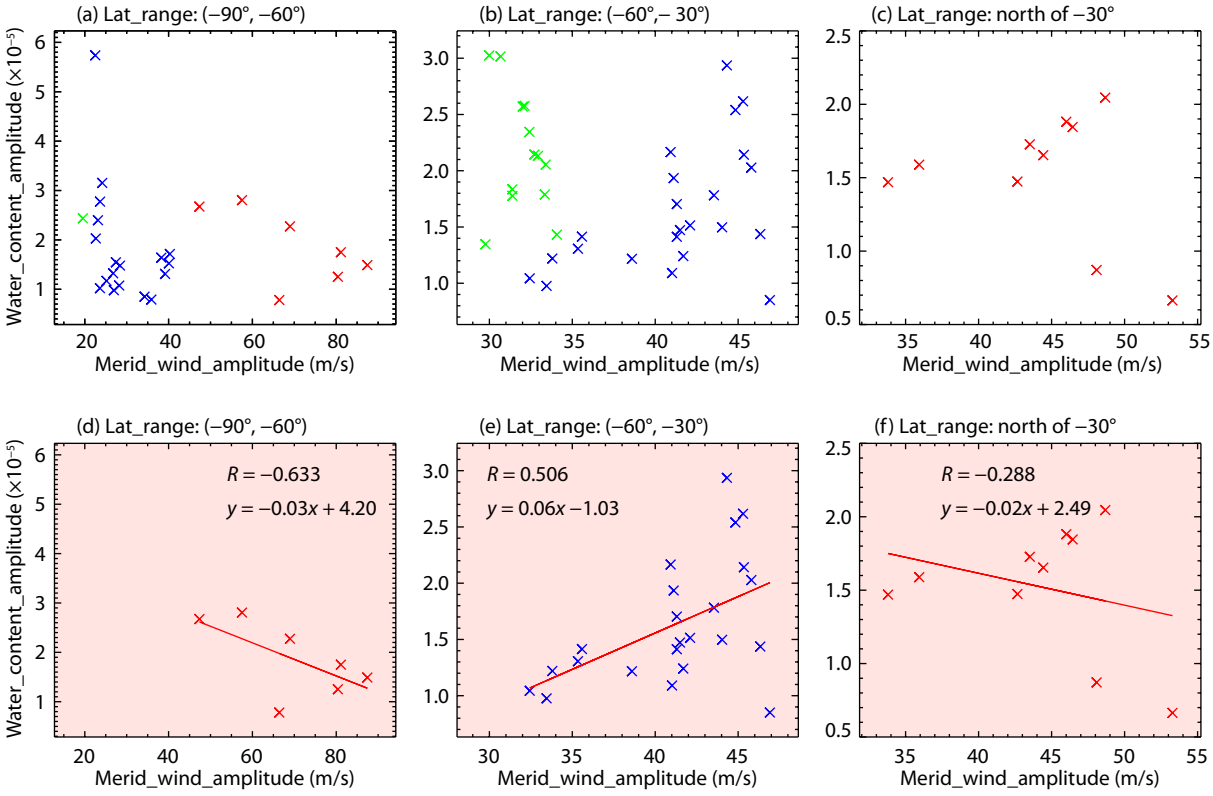

Figure 8. Same as Figure 5 but for the amplitudes of the meridional wind DW1 (*x*-axis) and amplitudes of the total water content abundance DW1 (*y*-axis).

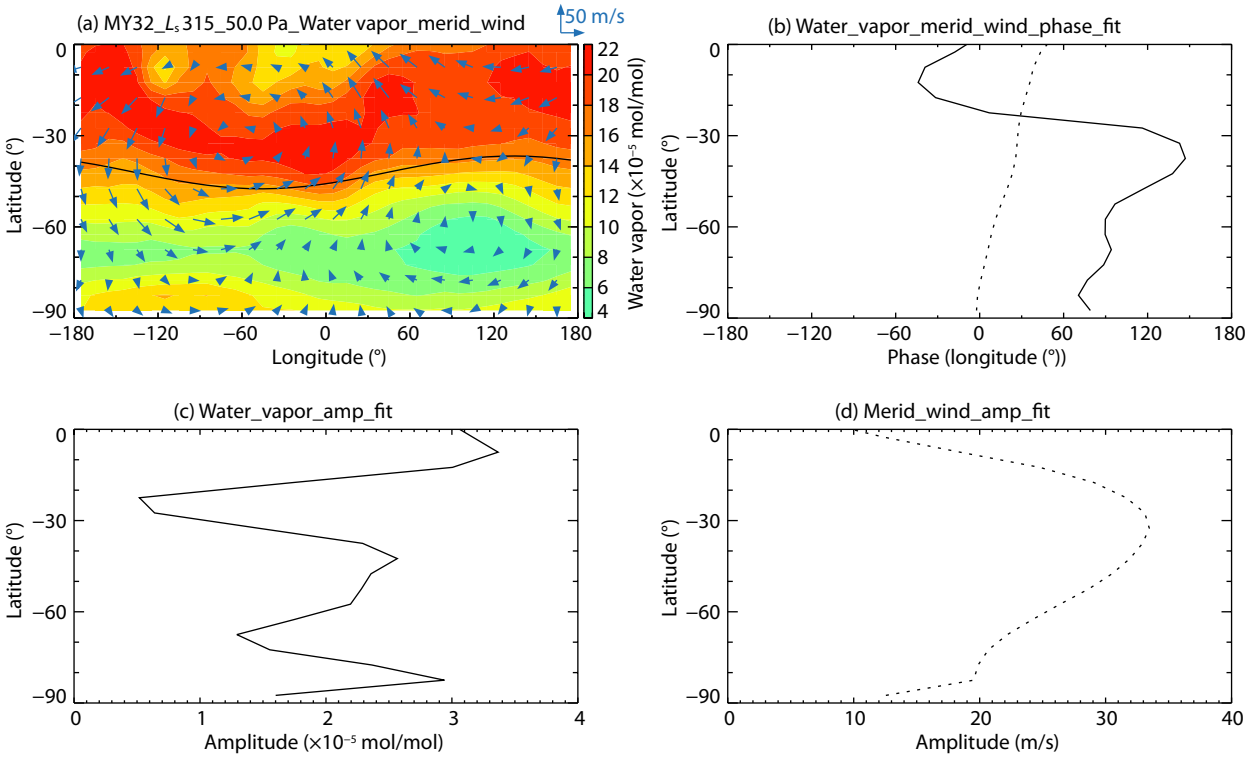

Figure 9. Latitudinal variations of the DW1 amplitudes (c, d) and phases (b) of water vapor (solid lines in b and c) and meridional wind (dotted lines in b and d) at 50 Pa, L_s of 315° during a C regional dust storm in MY 32. The black curve in (a) represents the fitted water vapor front.

ciated with the meridional wind DW1 is common during major dust storms. Compared with the water vapor abundance, the water vapor front is more representative of meridional water vapor transport. A water vapor front can be regarded as a meridional interface between high and low water vapor zones (Figures 1 and 3), which are highly dependent on the meridional distribution of water vapor. Because the different types of major dust storms usually occur in different seasons (Table 1), the latitudinal variation of the water vapor front during different dust storms (Figure 4) is related to seasonal variation in the water vapor distribution. Therefore, the effect of the tidal transport of water vapor should vary with the types of dust storms in different seasons.

The "climatology" dust scenario in the MCD is derived from the available observations of dust from MYs 24 to 32 without global dust storms. Thus, the results of the climatology scenario can represent the average atmospheric state in multiple MYs. Here we show the seasonal variation in the water vapor distribution at 50 Pa from the climatology scenario of MCD 5.3 in Figure 10. Water vapor is mainly concentrated at low latitudes at the beginning of the southern spring (L_s of 180°), but it gradually moves southward as the dust storm season begins and covers the middle latitudes from L_s of ~240°. During the southern summertime (L_s of ~250°–310°), the water vapor increases rapidly at high latitudes because of sublimation of the water ice in the polar caps (Trokhimovskiy et al., 2015), and it forms a peak two times larger than that at the mid- to low latitudes. After the southern summer solstice, the water vapor begins to move northward from the middle latitudes and concentrates again at low latitudes during the southern fall equinox. The seasonal variation of water vapor in Figure 10 was also found in previous observational studies (Fedorova et al., 2006; Trokhimovskiy et al., 2015). All the central latitudes of water vapor fronts during nonglobal dust storms (shown by blue and green crosses in Figure 10) are near the border of the area of high water vapor abundance (between the yellow and cyan areas). Thus, the central latitude of the water vapor front for a certain example is related to its corresponding L_s (Figure 4). In contrast, considering the limited amplitude of the water vapor front DW1 (no more than 10°), the tidally driven meridionally diurnal motion of water vapor during the non-dust-storm condition induces only a limited change to the meridional distribution of water vapor from its climate state.

In contrast, the water vapor front during global dust storms is far away from the climatological border of the area of high water vapor abundance. The two global dust storms in our analysis can further be divided into two types: the southern spring global dust storm (L_s of 190°–250° in MY 25) and the southern summer global dust storm (L_s of 265°–305° in MY 28). As shown in Figure 10, the water vapor fronts during the MY 28 southern summer global dust storm are mostly distributed at low latitudes, very far north of the climatological border of the high water vapor area, whereas those during the MY 25 southern spring global dust storm are distributed at high latitudes, far south of the climatological water vapor border. Typical examples of the diurnal variations in water vapor and wind fields during these two types of global dust storms are shown in Figure 4k and 4l. To make the transport process clearer, we abstracted Figure 4k and 4l as the concept diagram shown in Figure 11. During the MY 28 global dust storm (Figure 11b), the nightside tidal wind is able to transport water vapor from the high-latitude reservoir all the way to the low latitudes. As Wu ZP et al. (2020) discussed, in the period from noon to early afternoon (10:00–15:00 LT), when dusty deep convection is expected to be the strongest, the water vapor is retreating to higher latitudes from the equatorial region driven by the daytime southward tidal wind. In the intervening time, a considerable amount of water still remains in the mid- to low latitudes (0° to 60°S), which makes it highly susceptible to lifting by deep convection. However, the situation in the MY 25 global dust storm shown in Figure 11a behaves to the contrary. The daytime tidal wind

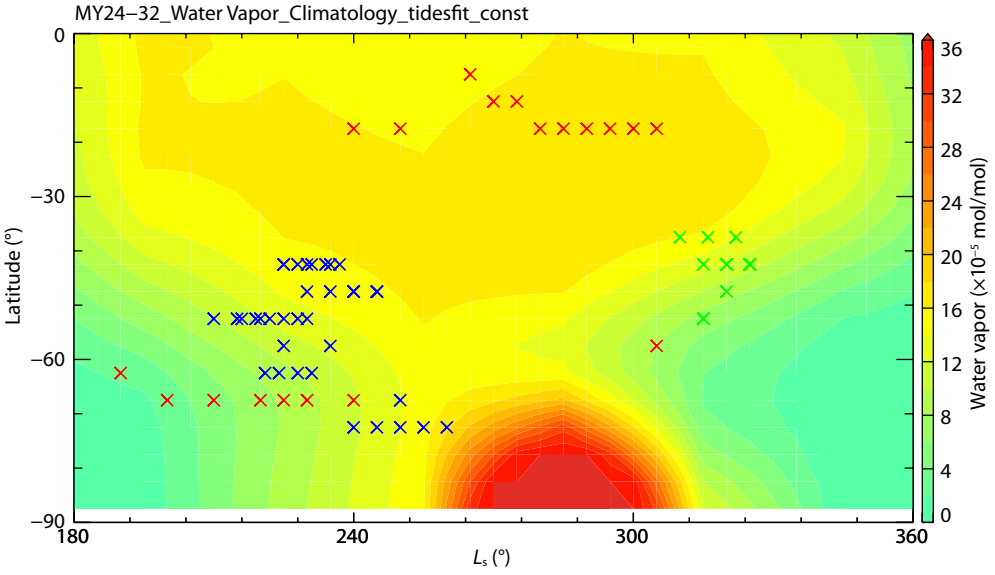

Figure 10. Climatology of the zonal mean water vapor abundance and the water vapor front distribution in different types of dust storms at 50 Pa in the southern hemisphere during the dust storm seasons (180°–360°). The blue, green, and red crosses represent the central latitudes of the water vapor front for samples of the A and C regional and global dust storms, respectively.

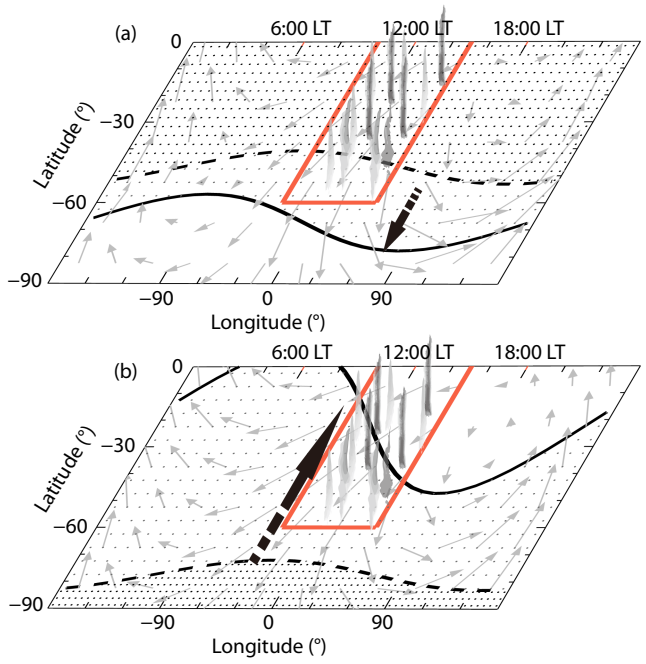

Figure 11. Conceptual diagram of the possible coupling process between horizontal tidal transport and vertical deep convection during (a) the MY 25 southern spring global dust storm and (b) the MY 28 southern summer global dust storm. The black dashed and solid lines indicate the water vapor front during the non-dust-storm condition and the global dust storm condition, respectively. The dense and sparse gray dots represent the relatively higher and lower concentrations of water vapor in the non-dust-storm versus global dust storm condition, respectively. The gray vectors represent the diurnal wind pattern. The red box shows the rough latitude (0°–60°S) and local time range (10:00–15:00 LT) where deep convection activities (vertical art vectors) are mostly expected to occur, based on Wang C et al. (2018) and Heavens et al. (2019).

transports water vapor from the mid- to low latitudes southward toward the high latitudes. Because deep convection occurs mainly at the mid- to low latitudes (Wang C et al., 2018; Heavens et al., 2019), this process decreases the water vapor abundance that can be lifted by deep convection.

In general, the meridional tidal wind during global dust storms can help spread water vapor from areas of higher abundance to areas of lower abundance, but in different directions for different global dust storms. Consequently, the MY 28 southern summer global dust storm increases the abundance of daytime water vapor at the mid- to low latitudes, whereas the MY 25 southern spring global dust storm decreases it. Eventually, the coupling between tidal transport and deep convection during the two global dust storms causes completely opposite effects on Martian water escape.

5. Concluding Remarks

Recent observations of the water vapor abundance in the Martian atmosphere have revealed an increase in atmospheric water vapor at altitudes as high as 80 kilometers during major dust storms (Heavens et al., 2018; Vandaele et al., 2019). Such high-altitude water vapor is thought to be lifted by a strong, deep convection process under dust storm conditions (Heavens et al., 2018, 2019). Wu ZP et al. (2020) proposed that during the global dust storm in MY 28, water vapor from the southern polar reservoir can be transported by the tidal wind to the mid- to low latitudes and lifted to high altitudes by deep convection. The positive performance of the MCD in short-period atmospheric dynamics during major dust storms offers the opportunity to systematically investigate tidally driven water vapor transport.

In this work, a pre-research study was conducted on the horizontal transport of water vapor during various major dust storms based on MCD 5.3. We investigated the horizontal motion of water vapor and its relationship to the meridional tidal wind in all the major dust storms from MYs 24 to 32. Similar to the commonly existing dust tides, a westward-propagating diurnal pattern in the water vapor front is prominent during nearly all the major dust storms. To quantitatively determine the characteristics of the diurnal motion of water vapor and its relationship to the tidal meridional winds, we used the nonlinear least-squares fit procedure to calculate the amplitudes and phases of the DW1. Under the ideal assumption that water vapor is transported only meridionally by the meridional wind DW1, the phase of the water vapor abundance–water vapor front DW1 should lag behind the phase of the meridional wind DW1 by roughly one-fourth of the DW1 period, and the amplitude of the water vapor front DW1 should be positively correlated with the amplitude of the meridional wind DW1 by a proportional coefficient of ~0.24°/(m/s). With these two criteria, we conducted statistical and correlation analyses for the water vapor abundance–water vapor front DW1 and the meridional wind DW1 based on ~70 samples collected during major dust storms. Before the analysis, all the samples were grouped into three latitude zones (high latitudes [–90°, –60°], middle latitudes [–60°, –30°], and low latitudes [north of –30°]) based on the central latitude of the water vapor front. The phase relationship between the water vapor abundance–water vapor front DW1 and the meridional wind DW1 in middle-latitude A regional dust storms and high-latitude and low-latitude global dust storms satisfies the phase-lagging criterion well, which provides direct evidence for tidally driven meridional transport of water vapor. Regarding its relationship with amplitude, the water vapor front DW1 has a more positive correlation with the meridional wind DW1, but the water vapor abundance DW1 does not because it is sensitive to other factors, such as the phase transition with water ice, the vertical transport effect, and the aliasing of its seasonal variation. Neither the amplitude nor phase relationship for the C regional dust storms is able to satisfy the criteria, indicating that other processes, such as tidal or planetary waves with shorter zonal wavelengths, may be as important as the migrating diurnal tide during C regional dust storms.

The latitudinal variation of the water vapor front during different dust storms is related to seasonal variation in the spatial distribution of water vapor. Therefore, the effect of the tidal transport of water vapor should vary with the type of dust storm in different seasons. Our analysis suggests that the tidal transport of water vapor during regional dust storms induces only a limited change to the meridional distribution of water vapor from its climate state,

whereas the tidal transport of water vapor during global dust storms can help spread water vapor from areas of higher abundance to areas of lower abundance. The water vapor abundance at mid- to low latitudes is susceptible to lifting by deep convection, which is directly linked to Martian water escape (Heavens et al., 2019). Because the tidal wind in the MY 28 southern summer global dust storm tends to increase the abundance of daytime water vapor at the mid- to low latitudes whereas that in the MY 25 southern spring global dust storm decreases it, the tidal transport process during these two types of global dust storms can cause opposite effects on Mars water escape.

Measurements for vertical profiles of water vapor in the Martian middle atmosphere are rare, especially for global dust storms. Recent studies based on observational data have revealed a rapid and significant increase in water vapor at altitudes as high as 80 km during the MY 28 and MY 34 global dust storms (Fedorova et al., 2018; Heavens et al., 2018; Vandaele et al., 2019). Although the data were collected by different instruments and associated retrieval procedures, which reduces their reliability for a direct comparison, it is still intriguing that the observed mixing ratio of the water vapor volume in the middle atmosphere during the MY 28 southern summer global dust storm (shown in Figure 6 by Fedorova et al., 2018) is higher than that during the MY 34 southern spring global dust storm (shown in Figure 2 by Vandaele et al., 2019) by an order of magnitude. Whether the coupling between deep convection and tidal transport would make a difference in water escape during different global dust storms is presently an open question. Further observations on globally diurnal variations in water vapor during major dust storms on Mars are needed in the future.

Acknowledgments

This work is supported by the B-type Strategic Priority Program of the Chinese Academy of Sciences (grant XDB41000000) and the pre-research project on Civil Aerospace Technologies of the China National Space Administration (grant D020105). T. L. and J. C. acknowledge support from the National Natural Science Foundation of China through grants 41525015 and 41774186 to J. C., and grants 41674149 and 41974175 to T. L. X. Z. acknowledges support from the National Science Foundation (grant AST1740921). J. L. acknowledges support from the Open Research Program of the Chinese Academy of Sciences Key Laboratory of Geospace Environment. Z. W. acknowledges support from the Guangdong Basic and Applied Basic Research Foundation (grant 2019A1515110815) and the Chinese Academy of Sciences Key Laboratory of Lunar and Deep Space Exploration (grant LDSE201803). We would like to thank the MCD teams for making the MCD 5.3 data sets available online at http://www-mars.lmd.jussieu.fr/mars/access.html.

References

Bandfield, J. L. (2007). High-resolution subsurface water-ice distributions on Mars. *Nature*, *447*(7140), 64–67. https://doi.org/10.1038/nature05781

Bibring, J. P., Langevin, Y., Poulet, F., Gendrin, A., Gondet, B., Berthé, M., Soufflot, A., Drossart, P., Combes, M., … the OMEGA team. (2004). Perennial water ice identified in the south polar cap of Mars. *Nature*, *428*(6983), 627–630. https://doi.org/10.1038/nature02461

Chaffin, M. S., Chaufray, J. Y., Stewart, I., Montmessin, F., Schneider, N. M., and Bertaux, J. L. (2014). Unexpected variability of Martian hydrogen escape. *Geophys. Res. Lett.*, *41*(2), 314–320. https://doi.org/10.1002/2013gl058578

Chaffin, M. S., Deighan, J., Schneider, N. M., and Stewart, A. I. F. (2017). Elevated atmospheric escape of atomic hydrogen from Mars induced by high-altitude water. *Nat. Geosci.*, *10*(3), 174–178. https://doi.org/10.1038/ngeo2887

Chapman, S., and Lindzen, R. S. (1970). *Atmospheric Tides* (pp. 200). Dordrecht, Netherlands: Springer. https://doi.org/10.1007/978-94-010-3399-2

Craddock, R. A., and Howard, A. D. (2002). The case for rainfall on a warm, wet early Mars. *J. Geophys. Res.: Planets*, *107*(E11), 5111. https://doi.org/10.1029/2001JE001505

Fedorova, A., Korablev, O., Bertaux, J. L., Rodin, A., Kiselev, A., and Perrier, S. (2006). Mars water vapor abundance from SPICAM IR spectrometer: Seasonal and geographic distributions. *J. Geophys. Res.: Planets*, *111*(E9), E09S08. https://doi.org/10.1029/2006JE002695

Fedorova, A., Bertaux, J. L., Betsis, D., Montmessin, F., Korablev, O., Maltagliati, L., and Clarke, J. (2018). Water vapor in the middle atmosphere of Mars during the 2007 global dust storm. *Icarus*, *300*, 440–457. https://doi.org/10.1016/j.icarus.2017.09.025

Forbes, J. M. (1995). Tidal and planetary waves. In R. M. Johnson, et al. (Eds.), *The Upper Mesosphere and Lower Thermosphere: A Review of Experiment and Theory* (pp. 67-87). Washington, DC: AGU. https://doi.org/10.1029/GM087p0067

Forget, F., Hourdin, F., Fournier, R., Hourdin, C., Talagrand, O., Collins, M., Lewis, S. R., Read, P. L., and Huot, J. P. (1999). Improved general circulation models of the Martian atmosphere from the surface to above 80 km. *J. Geophys. Res.: Planet*, *104*(E10), 24155–24175. https://doi.org/10.1029/1999je001025

Guzewich, S. D., Talaat, E. R., Toigo, A. D., Waugh, D. W., and McConnochie, T. H. (2013). High-altitude dust layers on Mars: Observations with the thermal emission spectrometer. *J. Geophys. Res.: Planets*, *118*(6), 1177–1194. https://doi.org/10.1002/jgre.20076

Guzewich, S. D., Wilson, R. J., McConnochie, T. H., Toigo, A. D., Banfield, D. J., and Smith, M. D. (2014). Thermal tides during the 2001 Martian global-scale dust storm. *J. Geophys. Res.: Planets*, *119*(3), 506–519. https://doi.org/10.1002/2013je004502

Haberle, R. M., McKay, C. P., Schaeffer, J., Cabrol, N. A., Grin, E. A., Zent, A. P., and Quinn, R. (2001). On the possibility of liquid water on present-day Mars. *J. Geophys. Res.: Planets*, *106*(E10), 23317–23326. https://doi.org/10.1029/2000JE001360

Haberle, R. M., Clancy, R. T., Forget, F., Smith, M. D., and Zurek, R. W. (2017). *The Atmosphere and Climate of Mars*. Cambridge: Cambridge University Press. https://doi.org/10.1017/9781139060172

Hale, A. S., Bass, D. S., and Tamppari, L. K. (2005). Monitoring the perennial Martian northern polar cap with MGS MOC. *Icarus*, *174*(2), 502–512. https://doi.org/10.1016/j.icarus.2004.10.033

Heavens, N. G., Johnson, M. S., Abdou, W. A., Kass, D. M., Kleinböhl, A., McCleese, D. J., Shirley, J. H., and Wilson, R. J. (2014). Seasonal and diurnal variability of detached dust layers in the tropical Martian atmosphere. *J. Geophys. Res.: Planets*, *119*(8), 1748–1774. https://doi.org/10.1002/2014JE004619

Heavens, N. G., Kleinböhl, A., Chaffin, M. S., Halekas, J. S., Kass, D. M., Hayne, P. O., McCleese, D. J., Piqueux, S., Shirley, J. H., and Schofield, J. T. (2018). Hydrogen escape from Mars enhanced by deep convection in dust storms. *Nat. Astron.*, *2*(2), 126–132. https://doi.org/10.1038/s41550-017-0353-4

Heavens, N. G., Kass, D. M., Shirley, J. H., Piqueux, S., and Cantor, B. A. (2019). An observational overview of dusty deep convection in Martian dust storms. *J. Atmos. Sci.*, *76*(11), 3299–3326. https://doi.org/10.1175/Jas-D-19-0042.1

Hinson, D. P., and Wilson, R. J. (2004). Temperature inversions, thermal tides, and water ice clouds in the Martian tropics. *J. Geophys. Res.: Planet*, *109*(E1), E01002. https://doi.org/10.1029/2003je002129

Jakosky, B. M., and Phillips, R. J. (2001). Mars' volatile and climate history. *Nature*, *412*(6843), 237–244. https://doi.org/10.1038/35084184

Jeans, J. H. (1921). *The Dynamical Theory of Gases* (3rd ed). Cambridge: Cambridge University Press.

Kass, D. M., Kleinböhl, A., McCleese, D. J., Schofield, J. T., and Smith, M. D. (2016). Interannual similarity in the Martian atmosphere during the dust storm season. *Geophys. Res. Lett.*, *43*(12), 6111–6118.

https://doi.org/10.1002/2016GL068978

Kleinböhl, A., John Wilson, R., Kass, D., Schofield, J. T., and McCleese, D. J. (2013). The semidiurnal tide in the middle atmosphere of Mars. *Geophys. Res. Lett.*, *40*(10), 1952–1959. https://doi.org/10.1002/grl.50497

Kleinböhl, A., Spiga, A., Kass, D. M., Shirley, J. H., Millour, E., Montabone, L., and Forget, F. (2020). Diurnal variations of dust during the 2018 global dust storm observed by the Mars Climate Sounder. *J. Geophys. Res.: Planets*, *125*(1), e2019JE006115. https://doi.org/10.1029/2019JE006115

Madeleine, J. B., Forget, F., Millour, E., Montabone, L., and Wolff, M. J. (2011). Revisiting the radiative impact of dust on Mars using the LMD global climate model. *J. Geophys. Res.: Planets*, *116*(E11), E11010. https://doi.org/10.1029/2011je003855

Martin-Torres, F. J., Zorzano, M. P., Valentín-Serrano, P., Harri, A. M., Genzer, M., Kemppinen, O., Rivera-Valentin, E. G., Jun, I., Wray, J., … Vaniman, D. (2015). Transient liquid water and water activity at Gale crater on Mars. *Nat. Geosci.*, *8*(5), 357–361. https://doi.org/10.1038/ngeo2412

McCleese, D. J., Heavens, N. G., Schofield, J. T., Abdou, W. A., Bandfield, J. L., Calcutt, S. B., Irwin, P. G. J., Kass, D. M., Kleinböhl, A., … Zurek, R. W. (2010). Structure and dynamics of the Martian lower and middle atmosphere as observed by the Mars Climate Sounder: Seasonal variations in zonal mean temperature, dust, and water ice aerosols. *J. Geophys. Res.: Planets*, *115*(E12), E12016. https://doi.org/10.1029/2010je003677

McKay, C. P. (1997). The search for life on mars. In D. C. B. Whittet (Ed.), *Planetary and Interstellar Processes Relevant to the Origins of Life* (pp. 263-289). Dordrecht: Springer. https://doi.org/10.1007/978-94-015-8907-9_14

Millour, E., et al. (2018). *The Mars Climate Database* (*version 5.3*). Paper presented at From Mars Express to ExoMars Scientific Workshop. Madrid, Spain: ESA-ESAC.

Montabone, L., Forget, F., Millour, E., Wilson, R. J., Lewis, S. R., Cantor, B., Kass, D., Kleinböhl, A., Lemmon, M. T., … Wolff, M. J. (2015). Eight-year climatology of dust optical depth on Mars. *Icarus*, *251*, 65–95. https://doi.org/10.1016/j.icarus.2014.12.034

Nair, H., Allen, M., Anbar, A. D., Yung, Y. L., and Clancy, R. T. (1994). A photochemical model of the Martian atmosphere. *Icarus*, *111*(1), 124–150. https://doi.org/10.1006/icar.1994.1137

Navarro, T., Madeleine, J. B., Forget, F., Spiga, A., Millour, E., Montmessin, F., and Määttänen, A. (2014). Global climate modeling of the Martian water cycle with improved microphysics and radiatively active water ice clouds. *J. Geophys. Res.: Planets*, *119*(7), 1479–1495. https://doi.org/10.1002/2013je004550

Pollack, J. B., Kasting, J. F., Richardson, S. M., and Poliakoff, K. (1987). The case for a wet, warm climate on early Mars. *Icarus*, *71*(2), 203–224. https://doi.org/10.1016/0019-1035(87)90147-3

She, C. Y., Krueger, D. A., Yuan, T., and Oberheide, J. (2016). On the polarization relations of diurnal and semidiurnal tide in the mesopause region. *J. Atmos. Solar-Terr. Phys.*, *142*, 60–71. https://doi.org/10.1016/j.jastp.2016.02.024

Shirley, J. H., and Mischna, M. A. (2017). Orbit-spin coupling and the interannual variability of global-scale dust storm occurrence on Mars. *Planet. Space Sci.*, *139*, 37–50. https://doi.org/10.1016/j.pss.2017.01.001

Smith, M. D. (2008). Spacecraft observations of the Martian atmosphere. *Annu. Rev. Earth Planet. Sci.*, *36*, 191–219. https://doi.org/10.1146/annurev.earth.36.031207.124334

Trokhimovskiy, A., Fedorova, A., Korablev, O., Montmessin, F., Bertaux, J. L., Rodin, A., and Smith, M. D. (2015). Mars' water vapor mapping by the SPICAM IR spectrometer: Five martian years of observations. *Icarus*, *251*, 50–64. https://doi.org/10.1016/j.icarus.2014.10.007

Vandaele, A. C., Korablev, O., Daerden, F., Aoki, S., Thomas, I. R., Altieri, F., López-Valverde, M., Villanueva, G., Liuzzi, G., … ACS Science Team. (2019). Martian dust storm impact on atmospheric H_2O and D/H observed by ExoMars Trace Gas Orbiter. *Nature*, *568*(7753), 521–525. https://doi.org/10.1038/s41586-019-1097-3

Wang, C., Forget, F., Bertrand, T., Spiga, A., Millour, E., and Navarro, T. (2018). Parameterization of rocket dust storms on mars in the LMD martian GCM: Modeling details and validation. *J. Geophys. Res.: Planets*, *123*(4), 982–1000. https://doi.org/10.1002/2017je005255

Wang, H. Q., and Richardson, M. I. (2015). The origin, evolution, and trajectory of large dust storms on Mars during Mars years 24–30 (1999–2011). *Icarus*, *251*, 112–127. https://doi.org/10.1016/j.icarus.2013.10.033

Wilson, R. J., Neumann, G. A., and Smith, M. D. (2007). Diurnal variation and radiative influence of Martian water ice clouds. *Geophys. Res. Lett.*, *34*(2), L02710. https://doi.org/10.1029/2006gl027976

Wu, Z. P., Li, T., and Dou, X. K. (2015). Seasonal variation of Martian middle atmosphere tides observed by the Mars Climate Sounder. *J. Geophys. Res.: Planets*, *120*(12), 2206–2223. https://doi.org/10.1002/2015JE004922

Wu, Z. P., Li, T., and Dou, X. K. (2017). What causes seasonal variation of migrating diurnal tide observed by the Mars Climate Sounder?. *J. Geophys. Res.: Planets*, *122*(6), 1227–1242. https://doi.org/10.1002/2017JE005277

Wu, Z. P., Li, T., Zhang, X., Li, J., and Cui, J. (2020). Dust tides and rapid meridional motions in the Martian atmosphere during major dust storms. *Nat. Commun.*, *11*(1), 614. https://doi.org/10.1038/s41467-020-14510-x

Zahnle, K., Haberle, R. M., Catling, D. C., and Kasting, J. F. (2008). Photochemical instability of the ancient Martian atmosphere. *J. Geophys. Res.: Planets*, *113*(E11), E11004. https://doi.org/10.1029/2008je003160